https://doi.org/10.5194/wes-2025-135
Preprint. Discussion started: 20 August 2025

Wind-tunnel analysis of wake-steering control strategies on a multi-column model wind farm

Derek Micheletto[1], Jens H. M. Fransson[1], and Antonio Segalini[2]

[1]FLOW, Dept. Eng. Mech., KTH Royal Institute of Technology, Stockholm, Sweden.
[2]Dept. Earth Sci., Geocentrum, Uppsala University, Uppsala, Sweden.

Correspondence: Derek Micheletto (derekm@kth.se)

Abstract. Wake-steering control has the potential of improving the power production of wind farms by deflecting the wakes of upstream turbines away from the downstream ones, thereby increasing the velocity impinging on the latter by sacrificing the performance of the former. In this work, a wide range of wake-steering control strategies are systematically applied to a 3×3 wind farm in a series of wind-tunnel experiments. When each streamwise column is operated identically to the others, the maximum measured power gain is approximately 5.3%. It is observed that the columns respond differently to a given yaw configuration, with the central one generally improving to a smaller degree than the lateral ones. Nevertheless, our data indicate that tuning each column independently of the others does not result in further power improvements. Furthermore, we show that increasing the free-stream velocity enhances the baseline power production of the model farm but reduces the scope for improvement achievable with wake-steering control.

1 Introduction

Turbine wake interactions are responsible for substantial power production losses in wind farms and constitute a key component of one of the grand challenges faced by the industry identified by Veers et al. (2019). Turbines affected by wake-impingement experience reduced incoming velocity and increased turbulence levels compared to those operating in the free stream. Consequently, clusters of turbines are less efficient than an equivalent number of isolated rotors and downstream turbines are subjected to greater fatigue loads. Given the prominent role that wind energy is expected to play in a future, decarbonized economy (International Energy Agency, 2024), control strategies aimed at mitigating the adverse wake effects have been the subject of extensive research. These involve modifying the operating conditions of certain turbines in order to influence the airflow within the wind farm, with the goal of maximizing the overall power output, minimizing the loads or achieving a balance between the two. A comprehensive review of wind farm flow control was recently provided by Meyers et al. (2022).

Strategies designed to increase the power output of the farm must address a tradeoff between the energy lost at the controlled turbines, which are operated in suboptimal conditions, and the energy gained at the downstream machines. These methods differ from the standard way of operating a wind farm, often termed "greedy", wherein each turbine is controlled to maximize its individual power production. The earliest approach, known as axial-induction control, consists of deregulating the upstream turbines, thereby reducing the velocity deficit in their wakes (Adaramola and Krogstad, 2011; Bartl and Sætran, 2016; van der Hoek et al., 2019; Bossanyi and Ruisi, 2021).

An alternative method is wake-steering control, which is the focus of this work. This approach leverages the horizontal deflection of the wake that occurs when a turbine is yawed with respect to the incoming wind direction. This deflection is induced by the spanwise component of the turbine thrust force that results from the misalignment and it can be exploited to direct the wake away from downstream rotors. This phenomenon was first observed in wind-tunnel experiments by Clayton and Filby (1982). Since then, the velocity deficit and the trajectory of the wakes of yawed turbines have been thoroughly studied, both numerically (Jiménez et al., 2010) and experimentally (Medici and Alfredsson, 2006).

Recent works have described more complex features of the structure of yawed wakes, such as the kidney-bean shape of the velocity deficit that develops in the cross-stream plane as a result of the formation of a counter-rotating vortex pair (CVP). This was observed in wind-tunnel experiments in the wake of a yawed porous disk by Howland et al. (2016) and behind a yawed turbine by Bastankhah and Porté-Agel (2016). The latter also explained, based on the mass budget analysis of the continuity equation, that the CVP is formed due to the large spanwise-velocity gradients found in such wakes. Furthermore, Bastankhah and Porté-Agel (2016) modeled the wake rotation and of the CVP as interacting vortices in a potential-flow framework. They found that the sense of the rotation of the wake relative to the direction of the CVP, in turn determined by the sign of the yaw angle, influences the magnitude of the lateral wake deflection and can also induce an upwards or downwards displacement. The LES simulations performed by Fleming et al. (2018) further demonstrated that the interaction between the wake rotation and the CVP leads to an asymmetry, with respect to the yaw direction of the upstream turbine, in the power available to a second turbine located downstream. A similar asymmetry was also documented by Bartl et al. (2018). Additionally, Fleming et al. (2018) observed that, when the wake of a yawed turbine interacts with that of a non-yawed turbine located downstream, it can induce a lateral displacement in the second wake. They termed this phenomenon secondary steering. Wang et al. (2018) later showed that the sidewash that accompanies the CVP and is responsible for secondary steering extends well outside the region of intense velocity deficit.

Dahlberg and Medici (2003) were among the first to examine the performance of two turbines in a wind tunnel while varying the yaw angle of the one upstream and traversing in the spanwise direction the one downstream. With their two-bladed rotors separated by three turbine diameters (D), they reported an overall power gain of about 10% when the upwind turbine was yawed by 20°. Similarly, Adaramola and Krogstad (2011) observed gains of 12% when their three-bladed turbines had the same streamwise spacing and the first one was yawed by 30°. Campagnolo et al. (2016) implemented a closed-loop, model-free control algorithm to maximize the output of three turbines separated by $4D$ in the streamwise direction and $0.5D$ in the spanwise direction. Yawing the two upstream turbines by approximately 20° and 16°, respectively, they obtained a 15% performance improvement. The influence of the relative position between turbines and of the turbulence intensity of the inflow on the maximum power gains achievable by active yaw control were examined by Bartl et al. (2018). In their experiments with two aligned turbines, the performance improvements ranged from 3.5 to 11%. The best results were obtained with a large streamwise distance and low inflow turbulence. Later, Bastankhah and Porté-Agel (2019) studied a broad range of yaw-angle combinations on a column of five aligned turbines with a longitudinal spacing of $5D$. They reported a maximum power gain

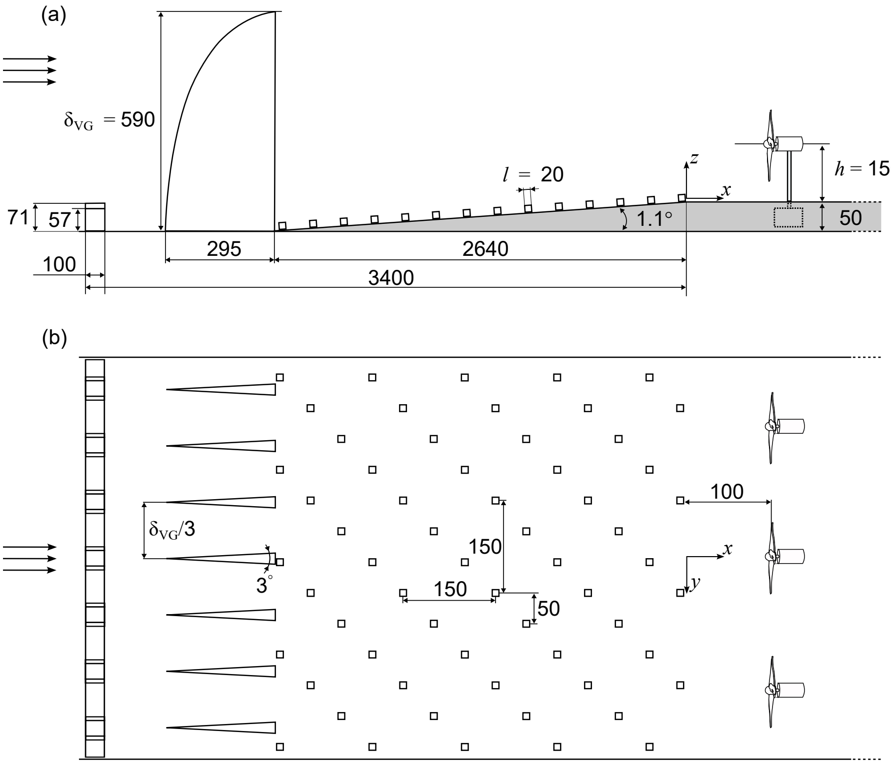

Figure 1. Side view (a) and top view (b) of the wind tunnel test section, not to scale. The flow is from left to right. The castellated barrier is placed at the inlet of the test section and the vortex generators are aligned with the castellations. The roughness elements are wooden cubes arranged in rows that are staggered in the lateral direction. Figure (a) also shows the foam boards positioned over the test section floor, with the concealed stepper motor installed at the base of the turbine tower depicted with a dashed line. All quotes are in millimeters.

of 17%, which reduced to 8% when only the first three turbines were considered. More recently, Rotea et al. (2024) conducted wind-tunnel experiments on a model farm consisting of 12 turbines arranged in four rows of three aligned columns. They compared performance improvements obtained with static tests and with a closed-loop controller. In both cases, they achieved performance improvements up to about 9%.

There have also been successful field studies involving full-scale machines. For example, Howland et al. (2019) reported a $7-13\%$ improvement on the performance of a farm consisting of six multi-MW turbines spaced by $3.5D$. More recently, Howland et al. (2022) performed a three-month long experiment on an array of three 2 MW turbines, separated by $4D$. For the range of wind directions in which wake-steering is relevant, their model-based controller achieved power gains of 1.2 to 3%, depending on the wind speed.

The wide ranges of performance improvements and of the yaw angles used to achieved them indicates that the efficacy of wake-steering control is highly dependent on multiple factors, including turbine characteristics, farm size and geometry, as well

https://doi.org/10.5194/wes-2025-135
Preprint. Discussion started: 20 August 2025

as inflow conditions. The nature of such dependencies, however, is not entirely understood. In this work, a large number of yaw-control configurations are systematically tested on a 3×3 aligned model wind farm in a series of wind tunnel experiments. The change in power production is examined at a farm, column and turbine level to identify the maximum power improvement and the range of angles necessary to achieve it. The effect of wake-steering on the turbine thrust force and fatigue loads is also examined on selected turbines. Finally, the influence of the inflow conditions is studied by gradually increasing the free-stream velocity. This article is structured as follows: Sect. 2 describes the experimental setup, including the devices used to replicate a neutrally-stable atmospheric boundary layer in the wind tunnel, the turbine models and the experimental procedure used to study the farm configurations. The results are presented in Sect. 3, analyzing first the impact of wake-steering control on the power production and then on the thrust force. The effects of increasing the free-stream velocity are discussed in Sect. 3.3 and those of tuning each column independently in Sect. 3.4. A comparison between our results and those from similar wind-tunnel studies on wake-steering control found in the scientific literature is presented in Sect. 4. Finally, the conclusions of this work are summarized in Sect. 5.

2 Methods

2.1 Wind tunnel

The experimental campaign was conducted in the Minimum Turbulence Level (MTL) wind tunnel at KTH. The closed-loop facility has a $7\ \mathrm{m}$ long test section with a $1.2 \times 0.8\ \mathrm{m}^2$ cross section and is powered by a $86\ \mathrm{kW}$ fan. A heat exchanger in the return channel, governed by a PID controller, regulates the air temperature inside the tunnel with a $\pm 0.05\ ^\circ\mathrm{C}$ precision. A more detailed description of the facility can be found in Lindgren and Johansson (2002). With an empty test section, the airflow in the wind tunnel is uniform and laminar, with a streamwise turbulence intensity less than 0.025%. To simulate the inflow conditions typically experienced by full-scale wind turbines, the thin boundary layer that develops naturally over the wind-tunnel floor was thickened using the method described by Counihan (1969). Thus, a castellated barrier was placed at the inlet of the test section, followed by seven vortex generators (VGs) and then by an array of roughness elements. Figure 1 shows a sketch of the test section, from the inlet to the first row of turbines. The height of the VGs, closely related to the expected depth of the replicated ABL, is $\delta_{\mathrm{VG}} = 590\ \mathrm{mm}$. The lateral distance between VGs and their wedge angle are $0.3\ \delta_{\mathrm{VG}}$ and $3°$, respectively. According to Hohman et al. (2015), these values promote a higher degree of spanwise homogeneity compared to the ones originally presented by Counihan (1969), at a given streamwise position. In addition, several foam boards were placed over the tunnel floor to conceal the wind turbine supports from the airflow. The boards beneath the roughness fetch were cut at an angle, forming a $1.1°$ slope, while the subsequent ones were of constant height. The ceiling of the test section was then adjusted to ensure a zero pressure gradient along the portion of the test section housing the wind turbines. The origin of the coordinate system used in this work is found at the end of the roughness fetch along the wind tunnel centreline, with $z = 0$ corresponding to the surface above the foam boards.

The simulated ABL was characterized in a prior campaign by means of hot-wire anemometry measurements, described in Micheletto et al. (2023b). The vertical profiles of the mean streamwise velocity component, U, and its standard deviation, u',

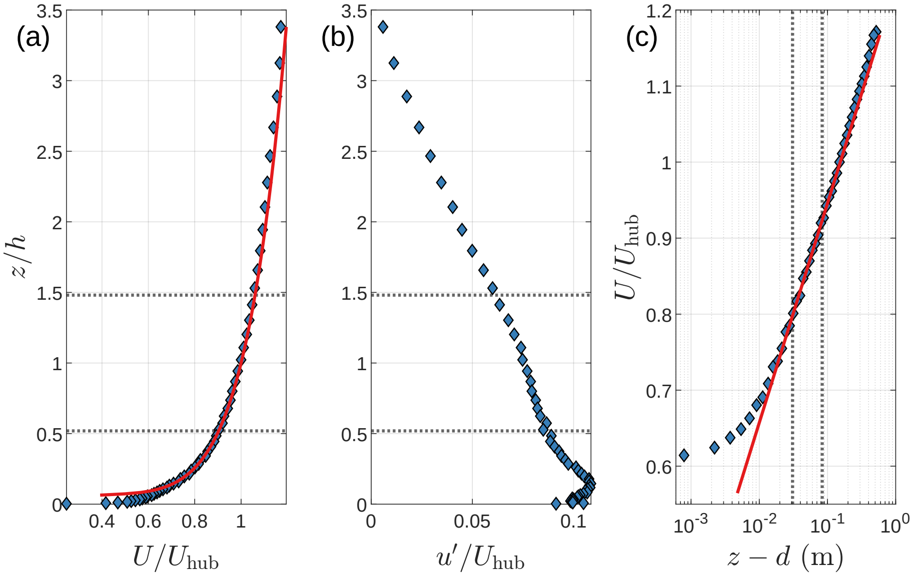

Figure 2. Mean streamwise velocity profile (a) and velocity standard deviation (b). The vertical coordinate z has been normalized with the turbine model hub height, $h = 156$ mm, while both U and u' have been normalized with the velocity measured at hub height, $U_{\mathrm{hub}} = U(z = h)$. The red line in (a) shows a power-law fit applied to the data points, whereas the one in (c) indicates a log-law fit of the type $u(z) = u^*/\kappa \, \ln[(z-d)/z_0]$ with $\kappa = 0.384$, $z_0 = 0.053$ mm, $d = 9.2$ mm and $u_\tau = 0.40$ m s^{-1}. The horizontal dotted lines in (a, b) delimit the rotor-swept area. The ones in (c) mark the region where the log-law fit was applied.

measured at $x = 100$ mm, are shown in Fig. 2(a) and (b). The boundary layer thickness, δ_{99}, which is defined as the distance from the wall at which the local mean velocity reaches 99% of the free-stream velocity, U_∞, is approximately 465 mm ≈ 3 h. The turbulence intensity at hub height is 7.5%. The mean velocity profile agrees reasonably well with a power-law fit applied to the data points within the interval $2l \leq z \leq 0.4\delta_{99}$. Here, the lower limit is used to remove the roughness sub layer from the fit (Bottema, 1997). The shear exponent obtained from the fit is $\alpha = 0.14$, a value typically encountered in turbulent boundary layers over a flat terrain with low vegetation (Counihan, 1975). Furthermore, Fig. 2(c) displays the mean velocity profile with semi-logarithmic scaling, illustrating its agreement with a log-law fit of the type $u(z) = u^*/\kappa \, \ln[(z-d)/z_0]$. The fit was performed using only the data measured in the range $2l \leq z \leq 0.2\delta_{99}$ and $\kappa = 0.384$ was used as the von Kármán constant (Österlund et al., 2000). The value of roughness length obtained from this procedure is $z_0 = 0.053$ mm, the displacement height is $d = 9.2$ mm (namely 46% of the roughness cube size) and the friction velocity is $u_\tau = 0.40$ m s^{-1}.

The spanwise profiles of the streamwise velocity component at five distinct heights are shown in Fig. 3. The footprint of the vortex generators is still visible as a series of high and low-speed regions in the upper three measurement locations. Closer to the ground, these oscillations are smoothed by the enhanced turbulent mixing provided by the roughness elements and the higher shear flow. The profiles also reveal that the flow velocity increases away from the centreline, leading to performance

https://doi.org/10.5194/wes-2025-135
Preprint. Discussion started: 20 August 2025

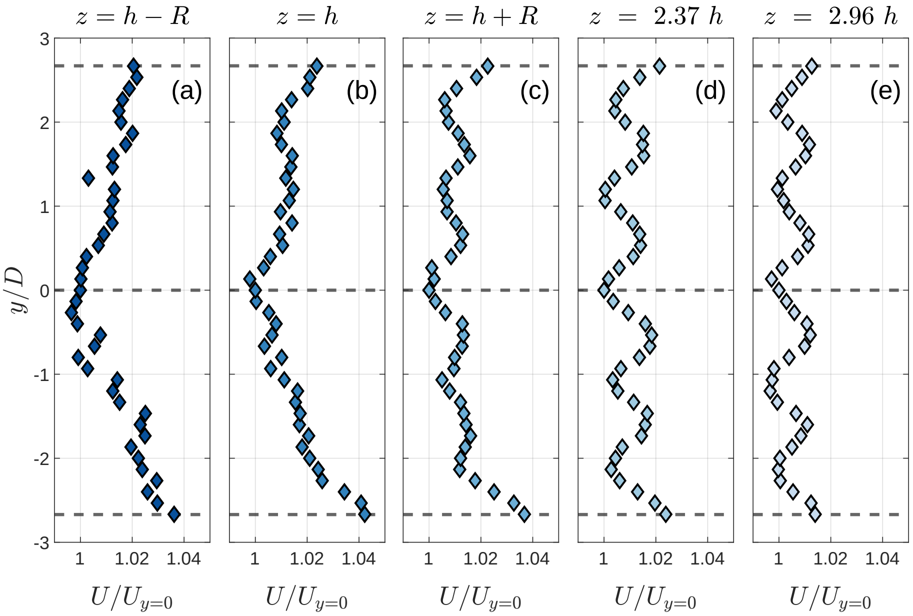

Figure 3. Spanwise profiles of the streamwise velocity component at five different heights, measured at $x = 100$ mm. The velocity has been normalized with the local value measured at the centreline of the test section. The profiles in Figs. (a) and (c) are taken at the upper and lower bounds of the rotor-swept area, while the one in (b) is measured at hub height. Figures (d) and (e) show profiles in the upper part of the ABL. The horizontal dashed lines indicate the spanwise locations where the farm columns are located.

variations among the turbines in different columns. Specifically, the column located at negative y experiences a free-stream velocity that is approximately 4% faster than that of the central column.

The velocity data presented in Figs. 2 and 3 was obtained with a free-stream velocity $U_\infty = 10\ \mathrm{m\ s^{-1}}$, whereas most of the experiments presented in this work were performed at $U_\infty = 7\ \mathrm{m\ s^{-1}}$, with an additional one at $8\ \mathrm{m\ s^{-1}}$ and one at $9\ \mathrm{m\ s^{-1}}$. The velocity profiles were not re-measured at these U_∞. However, in a preliminary experiment, a Prandtl tube was installed at $x = 0$, $y = 0$ and $z = h$ while a second one was mounted from the ceiling of the test section at $x = 0$, $y = 0$ and $z = 650$ mm. The free-stream velocity was then gradually increased from $7\ \mathrm{m\ s^{-1}}$ to $10\ \mathrm{m\ s^{-1}}$. It was observed that the ratio between the measured velocities remained approximately constant, i.e. $U_{\mathrm{hub}}/U_\infty = 0.85 \pm 0.005$, where the interval indicates the standard deviation. Based on this observation, it is assumed that the shape of the velocity profile at a given streamwise position remains independent of U_∞ in the range of U_∞ variation used here $\left(7 - 10\ \mathrm{m\ s^{-1}}\right)$. It is important to note that these measurements were performed before the installation of the model wind farm and it is not known how the velocity profiles and the spanwise homogeneity are affected by the farm blockage. Throughout this work, the power produced by the turbines will be normalized using the same velocity, namely the U_{hub} estimated from U_∞ that was measured with the Prandtl tube mounted through the test section ceiling at $x = 0$. This way, any error in the assumed U_{hub} is applied uniformly across all turbines and therefore does not affect the relative changes in power, which are the focus of this work.

https://doi.org/10.5194/wes-2025-135
Preprint. Discussion started: 20 August 2025

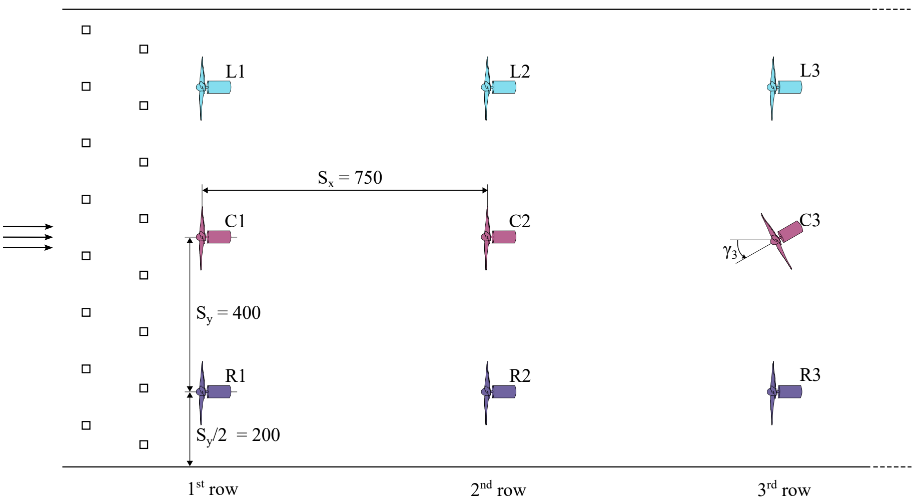

Figure 4. Top view of the wind-farm model, not to scale. The codes next to each turbine are used to identify them throughout this work. Similarly, the same colours will be used to identify the left, central and right column, respectively. Positive yaw angles are seen as counterclockwise when viewed from the top, as indicated for turbine T8.

2.2 Wind turbines

The nine wind-turbine models used in this work are three-bladed rotors with a diameter $D = 150$ mm. They are arranged in three columns aligned with the streamwise direction and three spanwise rows, separated in the streamwise direction by $S_x = 5D = 750$ mm. Within each row, the middle turbine is placed along the centreline of the test-section and the spanwise distance between the rotors is $S_y = 2.67D = 400$ mm. The distance between the lateral turbines and the sidewalls is $S_y/2$, so that each wall can be viewed as the reference surface separating the real farm from imaginary, specular farms limiting lateral confinement effects. Figure 4 contains a sketched top view of the farm and includes the numbers and letters used to identify each turbine throughout this work. The lateral columns, left and right, are named based on their position observed from an upstream perspective.

The turbine design follows the guidelines presented by Bastankhah and Porté-Agel (2017) for low Reynolds number applications (in the current study, $Re = U_{\mathrm{hub}}D/\nu = 59\,500$ for $U_\infty = 7\ \mathrm{m\ s^{-1}}$). The blade profiles are thus cambered flat plates with sharp leading and trailing edges. From an upstream perspective, they rotate in the counterclockwise direction. The turbines were 3D-printed in titanium as a single part, so the blade pitch angle is fixed. However, a pitch-angle variation study was conducted in an earlier campaign, using a prototype with adjustable blades. In light of the findings of those experiments, detailed in Mazzeo et al. (2022), the pitch angle of the current turbines is 2° larger than in Bastankhah and Porté-Agel (2017), as this geometry resulted in the highest power coefficient C_P. Each rotor hub is coupled with the shaft of a Faulhaber 2237S024CXR DC motor, here used as a generator, equipped with an IE3-32 rotary encoder which enables the measurement of turbine angular velocity Ω. The terminals of the generator are connected to an electrical circuit built in house for the dual purpose of moni-

https://doi.org/10.5194/wes-2025-135
Preprint. Discussion started: 20 August 2025

Figure 5. Photo of one of the turbine assemblies, displaying the rotor, the generator behind it, the tower with strain gauges and the stepper motor at the base.

toring the torque Q produced by the turbine and controlling Ω. The torque is linearly dependent on the current I through the external circuit, $Q = k_1 I + k_0$, which in turn is calculated from the measured voltage drop across an in-series resistor of known resistance. The coefficients k_0 and k_1 were determined by calibrating each motor using a disk of known inertia. Additionally, the external circuit includes a transistor system, controlled by an Arduino microcontroller, which modulates the electrical load applied to the generator, directly influencing I. This enables the digital regulation of the braking torque and therefore the control of the equilibrium angular velocity. A comprehensive description of the circuit is available in Micheletto et al. (2023a). The turbine hubs are mounted on top of aluminium towers at a height $h = 156$ mm. The base of each tower is secured to the shaft of a Sanyo Denki 103H5205-5040 stepper motor. Its rotation allows the control of the turbine yaw angle with an angular resolution of $1.8°$ per step. Using a second Arduino, the nine stepper motors can be controlled digitally and independently. As mentioned above, the stepper motors were positioned inside cutouts present in the foam panels and thus do not contribute to the turbine blockage. Finally, the three towers in the central column are equipped with a pair of strain gauges. These enable the measurement of the thrust force T along the rotor axis. A photo of the turbine assembly is presented in Fig. 5.

Although the nine rotors used in this study are nominally identical, the manufacturing process resulted in small geometrical differences (hardly visible to the naked eye) which are reflected on their power and thrust curves. Each turbine was tested individually, mounted at the position of C1 in Fig. 4 before any other tower had been installed in the wind tunnel. The mean values of the maximum power coefficients and of the corresponding optimal tip-speed ratios are $\overline{C}_{P,\max} = 0.34 \pm 0.01$ and $\overline{\lambda}_{\text{opt}} = 3.94 \pm 0.14$, where the intervals indicate the respective standard deviations. The mean thrust coefficient at $\overline{\lambda}_{\text{opt}}$ is $\overline{C}_T = 0.8 \pm 0.05$. The thrust and power curves shown in Fig. 6(a) and (b), respectively, correspond to the turbine in position

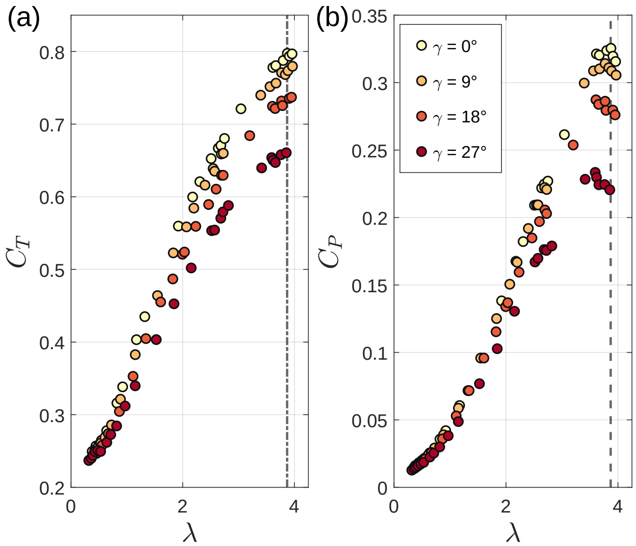

Figure 6. Thrust (a) and power (b) coefficient curves, as function of the tip-speed ratio and of the yaw angle, for turbine C3. The vertical dashed lines denote the optimal tip-speed ratio for $\gamma = 0°$.

C3. For this rotor, the maximum power coefficient measured at $\gamma = 0°$ is $C_{P,\max} = 0.325$ and it is achieved at the optimal tip-speed ratio $\lambda_{\text{opt}} = 3.87$. At these operating conditions, the thrust coefficient is $C_T = 0.797$.

2.3 Experimental procedure

The experiments presented in this work aim to evaluate the performance of the model wind farm under various yaw-angle configurations. This is achieved by measuring, for each configuration, the power output of every rotor, as well as the thrust force exerted on the turbines in the central column. To isolate the effects of wake-steering, every turbine must operate at the optimal tip-speed ratio $\lambda = \Omega R / U_{\text{hub}}$ which maximizes its power production. Such a requirement poses a challenge because the optimal Ω depends on the yaw angle and the value of U_{hub} impinging on the turbine, which is unknown a priori and varies from one configuration to another. This challenge holds for the wake-impinged turbines in the second and third rows, where the variations of the velocity deficit are significant, as well as for the ones in the first row, even though to a lesser degree, due to the upstream effects related to the farm blockage. To determine the optimal Ω for each turbine in every configuration, a gradient-based search algorithm was employed. The experimental procedure was as follows: initially, the yaw angles of the turbines in the first row were adjusted to the new configuration. Subsequently, the optimization algorithm was run in parallel on these turbines. This process was then repeated for the second and then for the third row. Finally, all analog signals were recorded for 90 s at a sampling frequency of 12 kHz using a NI9205 acquisition card. In addition, the free-stream velocity was measured, at each case, by means of the Prandtl tube mounted through the ceiling of the test section at $x = 0$ and connected to a Furness FCO560 differential manometer. The latter was also connected to a PT100 temperature probe and a PTX5072 pressure transmitter, used to acquire the ambient temperature and the atmospheric pressure. It should be noted that a preliminary test

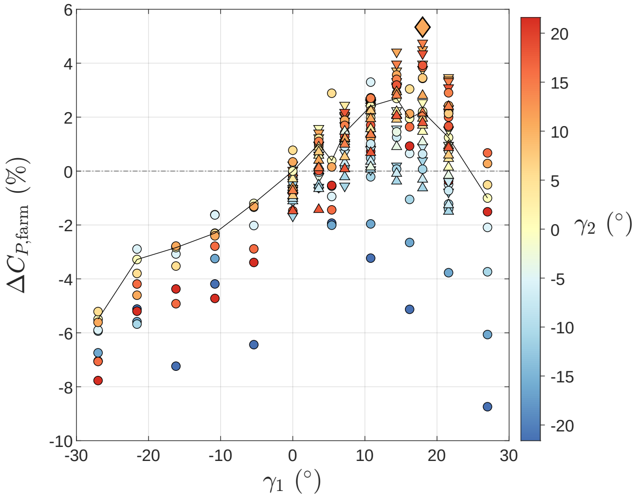

Figure 7. Normalized change of farm power coefficient of all the configurations. The abscissa and the color scheme denote the yaw angles of the first and second rows, respectively. The yaw angle of the third row is represented by different symbols: circles correspond to $\gamma_3 = 0°$, upward-pointing triangles indicate $\gamma_3 = 5.4°$ and downward-pointing triangles signify $\gamma_3 = -5.4°$. The black solid line links the configurations in which $\gamma_2, \gamma_3 = 0°$. The diamond symbol indicates the configuration resulting in the largest overall power improvement.

confirmed that performing the optimization in parallel for turbines in the same row leads to the same result as executing the routine for one turbine at a time. Naturally, the optimization cannot be performed on turbines in different rows, because it would entail changing the U_{hub} of the downstream rotors at every iteration. The yaw-angle actuation, the optimization of Ω and the data acquisition were all coordinated by a LabView program and the procedure took approximately $10\ \mathrm{min}$ per configuration. The repeatability of the optimization algorithm was evaluated by executing the procedure 30 times, cycling through three distinct configurations (including the greedy one). On average, the standard deviation of the farm power measured across 10 iterations per configuration was less than $0.5\ \%$ of the mean.

In order to reduce the number of degrees of freedom, and therefore the number of configurations to be tested, turbines in the same row are assigned the same yaw angle. This approach effectively treats the model farm as if it consisted of an infinitely large number of columns, with negligible edge effects. Thus, in this work, the variables γ_1, γ_2 and γ_3 will refer to the yaw angles of all the turbines located in the first, second and third rows, respectively. Each configuration will be identified by its angle vector, $\overline{\gamma} = (\gamma_1, \gamma_2, \gamma_3)$.

3 Results

3.1 Farm power

The response of the wind farm to wake-steering control was assessed in two experiments. In the first experiment, EXP1, a broad range of angles was tested with a coarse resolution and with the third-row turbines kept at $\gamma_3 = 0°$. This last condition was

Table 1. Ranges and resolutions of the yaw angles considered for each row of turbines in the two experiments. Each interval is defined as initial angle : step angle : final angle.

	EXP1	EXP2
γ_1	$-27^\circ : 5.4^\circ : 27^\circ$	$0^\circ : 3.6^\circ : 21.6^\circ$
γ_2	$-21.6^\circ : 5.4^\circ : 21.6^\circ$	$-10.8^\circ : 3.6^\circ : 18^\circ$
γ_3	0°	$-5.4^\circ, 0^\circ, 5.4^\circ$

Table 2. Yaw angles of the three rows and change of farm power coefficient of the five best configurations measured across the two experiments.

γ_1	γ_2	γ_3	$\Delta C_{P,\text{farm}}$
18°	10.8°	0°	$+5.3\ \%$
18°	14.4°	-5.4°	$+4.7\ \%$
18°	10.8°	-5.4°	$+4.5\ \%$
14.4°	10.8°	-5.4°	$+4.4\ \%$
18°	18°	-5.4°	$+4.3\ \%$

based on the assumption that aligning the third-row turbines with the incoming wind would maximize their power output and that the model farm would not benefit from their suboptimal operation. The second experiment, EXP2, was designed taking into account the insights gathered from EXP1. Consequently, the test matrix of EXP2 covered a narrower range of angles with a finer resolution. Additionally, the impact of yawing the third row was also investigated in EXP2. A summary of the configurations tested in each experiment is found in Table 1. The overall farm performance in each configuration is quantified by the farm-power coefficient, defined as $C_{P,\text{farm}} = \frac{1}{9}\sum_{i=1}^{9} C_{P,i}$, where $C_{P,i}$ represents the power coefficient of the i-th turbine. Note that all power coefficients were computed using the same reference velocity, $U_\text{hub} = 5.95\ \text{m s}^{-1}$, i.e. the undisturbed velocity at hub height upstream of the first row. Consequently, the coefficients of the turbines in the second and third row account for the losses due to wake interactions. The greedy configuration was measured multiple times distributed throughout each experiment, yielding a greedy farm-power coefficient $C_{P,\text{gr}} = 0.178 \pm 0.0015$. The corresponding array efficiency, which is computed as the ratio between $C_{P,\text{gr}}$ and the mean C_P, in the greedy configuration, of the three turbines in the first row, is approximately 58%.

Figure 7 displays $\Delta C_{P,\text{farm}}$ for all yaw-controlled configurations. This represents the normalized change in farm performance, relative to the greedy case:

$$\Delta C_{P,\text{farm}} = \frac{C_{P,\text{farm}} - C_{P,\text{gr}}}{C_{P,\text{gr}}} \times 100\ . \tag{1}$$

The figure reveals that the farm response to yaw control is strongly asymmetric with respect to the sign of γ_1. In fact, $\Delta C_{P,\text{farm}} < 0$ in all configurations with $\gamma_1 < 0^\circ$. This observation led to decision to consider only positive values of γ_1 in

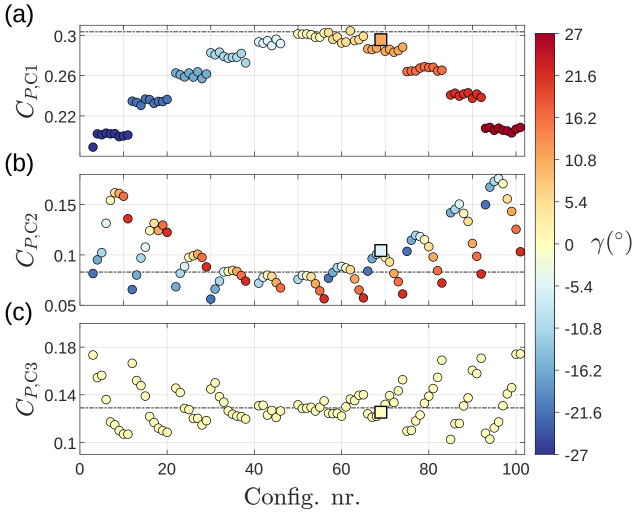

Figure 8. C_P of the central turbines C1 (a), C2 (b) and C3 (c), cf. Fig. 4. The abscissa denotes the configuration number, following the chronological order in which the configurations were tested. The color scheme represents the value of γ of the corresponding turbine. The horizontal dash-dotted lines indicate the C_P value in the greedy configuration. The square symbols highlight an example of a high-performing Type 2 configuration.

EXP2. The details of the five best-performing configurations are listed in Table 2. The optimum is found at $\overline{\gamma} = (18°, 10.8°, 0°)$ and corresponds to $\Delta C_{P,\mathrm{farm}} = +5.3\%$. A common feature among the best cases is that the magnitude of the yaw angles decrease progressively from row to row, a trend that was also observed by Bastankhah and Porté-Agel (2019). Furthermore, all listed configurations, except for the best overall, feature $\gamma_3 = -5.4°$, suggesting that it can be advantageous to yaw the trailing row of turbines, as well. It is also possible to distinguish two types of configurations: Type 1, in which the first two rows are both yawed in the positive direction, and Type 2, where $\gamma_2 < 0°$, i.e. with opposite sign to γ_1. While most of the best-performing configurations belong to Type 1, Fig. 7 shows that some cases leading to a positive $\Delta C_{P,\mathrm{farm}}$ fall into Type 2. This suggests that there are qualitatively different wake-steering strategies that result in a net power gain.

To fully understand these observations, it is necessary to examine in detail the response of the individual turbines and the behaviour of the columns under various configurations.

3.1.1 The central column

The power coefficients of the rotors in the central column are plotted in Fig. 8, in the chronological order in which the configurations were tested. Here, only the data from EXP1 is presented, as this is sufficient to visualize the trends discussed in this section. In Fig. 8(a) it is observed that $C_{P,\mathrm{C1}}$ remains relatively constant until γ_1 is changed, indicating that the operating conditions of the downstream rows have no influence. The value of $C_{P,\mathrm{C1}}$ decays roughly as $\cos^3(\gamma_1)$, as shown in Sect. 3.1.2 . Further downstream, $C_{P,\mathrm{C2}}$ exhibits a dual dependence on γ_1 and γ_2. For a given γ_1, $C_{P,\mathrm{C2}}$ changes as a cosine function of γ_2 and the maximum achievable $C_{P,\mathrm{C2}}$ increases with larger γ_1. Interestingly, the γ_2 value corresponding to each local maximum

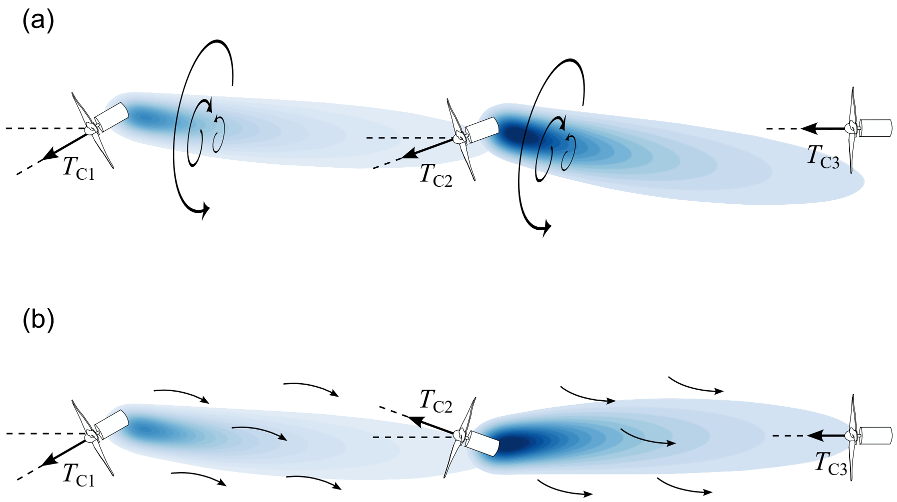

Figure 9. Qualitative representation of the most relevant flow phenomena in the two Types of yaw configurations: **(a)** Type 1, in which both γ_1 and γ_2 are positive and **(b)** Type 2, in which $\gamma_1 > 0°$ and $\gamma_2 < 0°$.

of $C_{P,\mathrm{C2}}$ is also dependent on γ_1: it has the opposite sign and its magnitude grows as $|\gamma_1|$ increases. Therefore, for a given γ_1, the cumulative power of C1 and C2 is maximized not by aligning the downstream turbine with the incoming wind direction, as intuition might suggest, but by yawing it in the opposite direction of the upstream turbine. This behaviour, which is also observed in the lateral columns, is in agreement with the findings of McKay et al. (2013) and of Bartl et al. (2018) for turbines operating in partial wakes. This finding prompted the inclusion of configurations with $\gamma_3 \neq 0°$ in EXP2. The most likely explanation is that the sidewash that accompanies the CVPs behind the first row of turbines induces a significant reorientation of flow upstream of the second row. As a result, when the turbines in the second row are yawed in the opposite direction as the ones in the first, they are effectively realigned with the local wind. This is illustrated in a qualitative sketch in Fig. 9(b). Considering that Wang et al. (2018) showed that the region of sidewash extends outside of the wake and that Fleming et al. (2018) observed constructive interactions between wakes and vortices of turbines within the same row, the spanwise velocity component may be further amplified due to the close spacing of the turbine columns in this experiment. Additionally, it is reasonable to expect that the flow downstream of C2, deflected in opposite directions by the first two turbines, becomes once again closely aligned with the column axis. Furthermore, it is reasonable to expect that the higher power extracted by C2 is accompanied by an increased thrust force T_{C2} (see Fig. 6), leading to a stronger velocity deficit upstream of C3. This explains why, in Type 2 configurations, the production of the turbines in the third row is lower than in greedy operation. Figure 8 presents an example of such a configuration, highlighted with square symbols, where $\gamma_1 = 10.8°$, $\gamma_2 = -5.4°$ and $\Delta C_{P,\mathrm{farm}} = +3.3\%$. This demonstrates

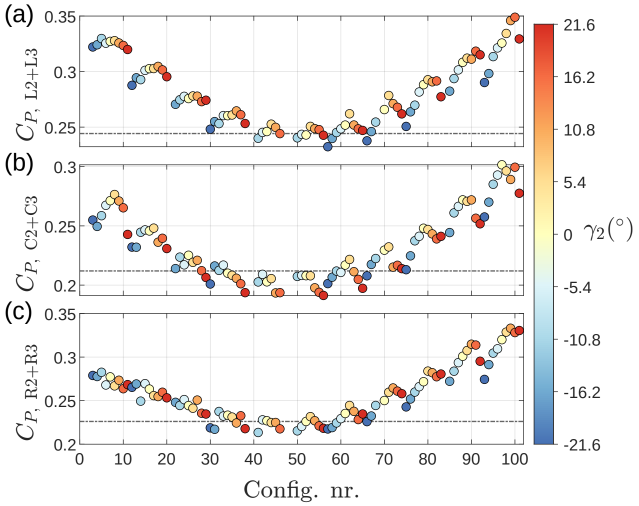

Figure 10. Sum of the C_P of the two downstream turbines in the left (a), central (b) and right column (c). The abscissas identify the configuration number in chronological order, as in Fig. 8. The color scheme represents the yaw angle of the turbines in the second row. The horizontal black lines represent the corresponding values in the greedy configuration.

that the farm power production can be increased by optimizing the collective performance of the first two rows, even if this improvement comes at the expense of the third.

In Type 1 configurations, where both γ_1 and γ_2 are positive, power production is more evenly distributed across all rows. This can be inferred by considering the sum of the C_P values of the two downstream turbines, illustrated for all columns in Fig. 10. For each γ_1, the cumulative power exhibits a similar trend to that of $C_{P,\text{C2}}$ seen in Fig. 8b, albeit less pronounced and with greater scatter in certain cases. Unlike $C_{P,\text{C2}}$, however, local maxima are more frequently observed at $\gamma_2 > 0°$, particularly when $\gamma_1 > 0°$ (Config. nr. 56 and above). This is in spite of the fact that, as stated above, the power of the second turbine would be higher if it were yawed in the negative direction while $\gamma_1 > 0°$. It follows that, in these configurations, the wind speed upstream of the third row is sufficiently high to more than compensate the missed production in the second row. This effect is likely driven by the interaction between the wake of the second turbine and the CVP and consequent sidewash of the first turbine, which results in an enhanced deflection of the second wake. This amplified deflection, induced by the yawed wake of the upstream turbine, may be understood as a generalization of the phenomenon known as secondary steering, described by Fleming et al. (2018).

Additionally, Fig. 10 shows that the sum of the downstream C_P is more sensitive to changes of γ_2 when $\gamma_1 > 0°$ (Config. nr. $\geq$ 56) than when $\gamma_1 < 0°$ (Config. nr. $<$ 56). This effect is particularly noticeable in the lateral columns, but it can also be observed at large magnitudes of γ_1 in the central column. This increased sensitivity suggests that the interactions between the wakes and CVPs of the upstream turbines with those of the second-row rotors are more effective when $\gamma_1 > 0°$. As a result, adjusting γ_2 in these cases can have a greater impact on the velocity deficit upstream of the third row, potentially leading to larger cumulative C_P. Conversely, these interactions are less prominent when $\gamma_1 < 0°$. In these cases, most of the additional

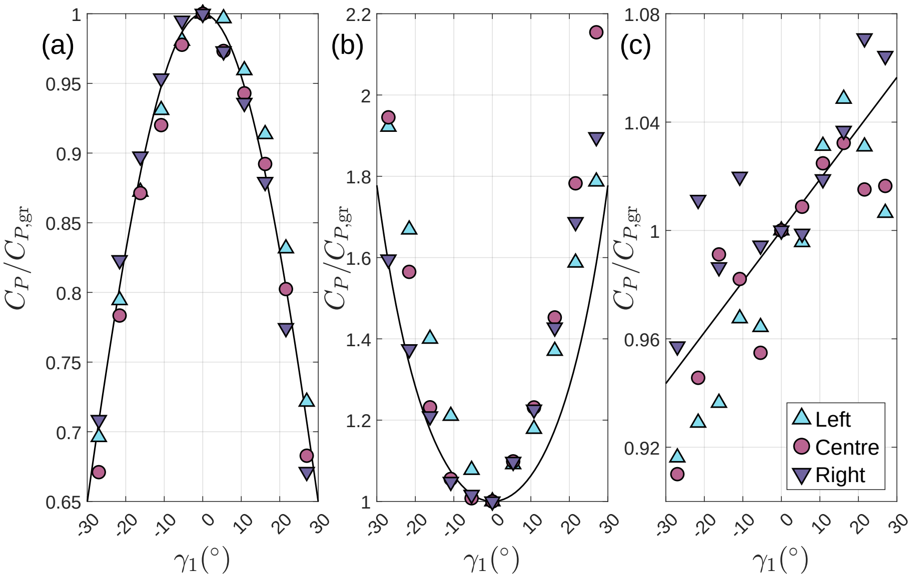

Figure 11. Variation of the power coefficients of the turbines in the first (a), second (b) and third row (c), normalized with the corresponding value in the greedy configuration and plotted as a function of γ_1. The size of the symbols is representative of the uncertainty related to the zero-alignment of the turbines, here assumed to be a single step of the stepper motors, i.e. 1.8°. The solid lines in Figs. (a), (b) and (c) represent the functions $\cos^3\gamma_1$, an arbitrary even function and a linear least-square fit, respectively. Note that the latter two are only used to assist the visualization.

power produced by the third-row turbines derives from the energy that was not extracted by the second-row rotors, and vice versa, leading to smaller variations of the cumulative C_P. Previous studies have found that the sense of rotation of the wake and the presence of the shear layer due to the ABL can result in larger wake deflection in one yaw direction than the other (Fleming et al., 2018; Zong and Porté-Agel, 2020). Additionally, Bastankhah and Porté-Agel (2016) showed that yawed turbine wakes also exhibit a vertical displacement, which can be pointed upwards or downwards depending on the yaw direction. These asymmetries in the deflection of the upstream turbine wakes, relative to the sign of γ_1, are therefore likely to modulate the wake steering of the second-row rotors. It should be noted that the low design tip-speed ratio and consequent high torque cause the wake rotation of the turbine models used in this study to be more pronounced compared to full-scale turbines operating at $\lambda \geq 6$ (Bourhis et al., 2022). As a result, the effects of wake interactions observed here may be somewhat accentuated. Nevertheless, the observation of similar asymmetries in wind-tunnel studies with turbines operating a higher tip-speed ratios (the model used by Bartl et al. (2018) operated at $\lambda = 6$) indicates that the trends identified here remain qualitatively relevant for full-scale applications.

3.1.2 The asymmetry in the farm response

The yaw direction of the turbines in the first row plays a major role in determining whether the farm power will increase or decrease in response to a wake steering strategy. As mentioned in Sect. 3.1, the model farm outperforms the greedy configuration only if $\gamma_1 > 0°$. This asymmetry is here investigated, restricting the analysis to the subset of the cases from EXP1 in which $\gamma_2 = \gamma_3 = 0°$, thus isolating the effect of γ_1. These cases are also highlighted in Fig. 7 (black solid line). The variation of the power coefficients of the turbines in the first, second and third row as a function of γ_1 are presented in Fig. 11(a), (b) and (c), respectively. As expected, the C_P values of the turbines in the first row diminish monotonically as $|\gamma_1|$ increases, closely following the empirical formula $C_P(\gamma) = C_P(\gamma = 0°)\cos^3(\gamma)$ found for example in Burton et al. (2011). A small asymmetry is already observable in the lateral columns. In fact, the power of the turbine in the left column decays more slowly (and the one in the right more rapidly) than what is predicted by the cosine relation for $\gamma_1 > 0°$. The opposite is true for for $\gamma_1 < 0°$. As the turbines in the first row are yawed further away from the wind direction, the power produced by the second row increases steadily and can even double as γ_1 approaches ±30°, as observed in Fig. 11(b). It can also be observed that the C_P of the turbines in the central and right columns increase faster when $\gamma_1 > 0°$. The turbine on the left column, on the other hand, exhibits a more symmetrical behaviour, except at large values of $|\gamma_1|$, where L2 performs better when $\gamma_1 < 0°$. The highest degree of asymmetry is observed in the third row. As seen in Fig. 11(c), the power coefficients increase almost linearly as γ_1 transitions from negative to positive values. Furthermore, yawing the first row at a negative angle generally leads to a performance reduction in the third-row turbines. This indicates that the sign of γ_1 has a moderate influence on the second-row turbines and plays a crucial role for the third row. The asymmetry in the second row likely stems from the aforementioned difference in deflection magnitude, for a given $|\gamma_1|$, which favours positive yaw angles. It should be noted that the preferred direction of yaw identified in the present experiment, i.e. counterclockwise when seen from the top, is in agreement with the findings of Bartl et al. (2018), whose turbines also rotated counterclockwise when seen from the front. The reverse trend observed for turbine L2 may be due to the fact that a negative γ_1 entails that the wake of turbine L1 is deflected away from the farm, rather than towards it, potentially offsetting the greater deflection observed for positive γ_1. Yet, the change in deflection magnitude alone is unlikely to fully account for response of the third row. A more plausible explanation involves the vertical displacement of the yawed wakes. When Bossuyt et al. (2021) compared the wakes of yaw and tilt-controlled turbines in wind tunnel experiments, they observed that the downward displacement induced by a negative tilt increases the available power at a downstream turbine by augmenting the downward transfer of kinetic energy. On the other hand, an upward deflection reduces the velocity impinging on the upper section of the downstream rotor. Considering that yaw misalignment can also induce a minor vertical deflection and that Bastankhah and Porté-Agel (2016) observed a downward displacement for positive yaw angles (adjusted for the different sign convention used in this work), this mechanism may provide a more comprehensive explanation for the impact of γ_1 on the third-row turbines. It is worth recalling that the turbine model employed by Bastankhah and Porté-Agel (2016) served as the basis for rotor geometry used in this work.

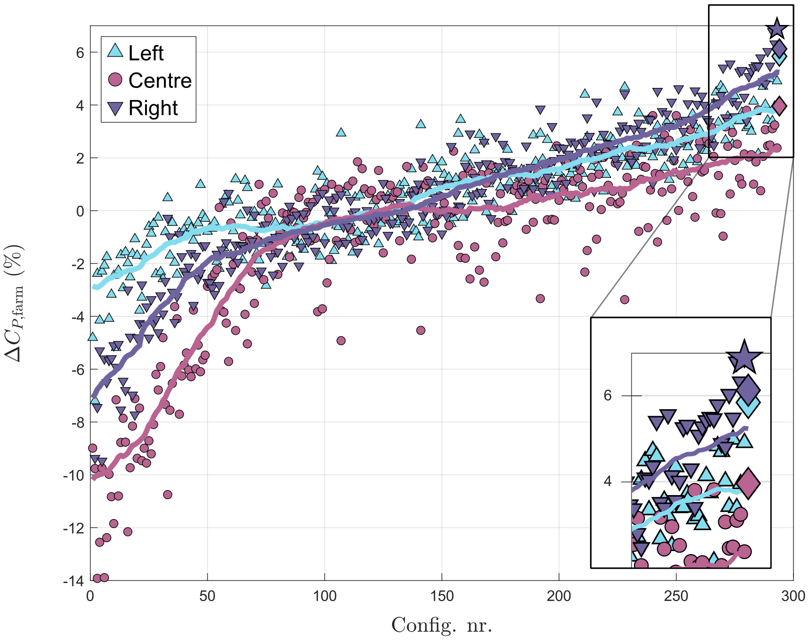

Figure 12. Change of the power coefficients of the three columns, relative to the the respective greedy values and sorted according to the total farm power, from worst to best. The solid lines indicate moving averages, whereas the diamond and pentagram symbols denote the farm-optimal and column-optimal cases, respectively. The inset provides a close-up of the best-performing configurations.

3.1.3 Difference between columns

The previous discussion highlighted that turbines within the same row have different responses to a given yaw configuration. In fact, the performance of each column is also affected differently. This is illustrated in Fig. 12, which displays the column power coefficient $C_{P,\mathrm{col}}$, defined as the average C_P of the turbines in a given column, for all the configurations tested in EXP1 and EXP2. Here, the configurations have been sorted in increasing order relative to the total farm power. The farm-optimal configuration, i.e. $\overline{\gamma} = (18°, 10.8°, 0°)$, is thus found at the right end of the plot. Interestingly, while this configuration also maximizes the $C_{P,\mathrm{col}}$ of the left and centre columns, the right column is optimized at a different configuration, namely $\overline{\gamma} = (18°, 14.4°, -5.4°)$. The improvements of left, centre and right columns in the farm-optimal case are 5.8%, 4% and 6.1%, respectively. This grows to 6.9% for the right column in its optimal case. Figure 12 also reveals that, in the majority of cases, the central column experiences a smaller improvement than the lateral ones. This is also the column which exhibits the lowest $C_{P,\mathrm{col}}$ in greedy operation, primarily because of the low performance of turbine C2, as will be further discussed in Sect. 3.3. Both observations may be partly attributed to the lower velocity measured in the center of the test section prior to farm installation (see Fig. 3(b)) and partly to the close spacing of the columns, which limits the entrainment of kinetic energy into the center of the array. The distribution of power within the columns corroborates this hypothesis: on average across the 15

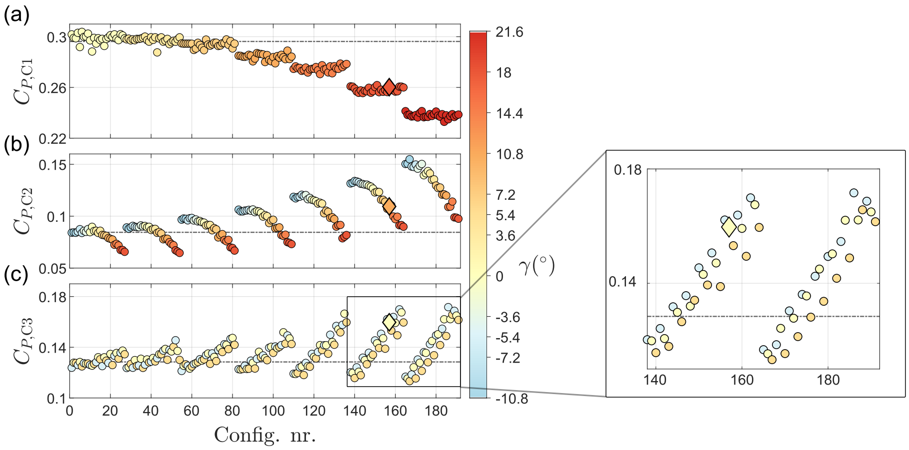

Figure 13. C_P of the central turbines C1 (a), C2 (b) and C3 (c), cf. Fig. 4. The abscissa identifies the configuration number, following the chronological order in which the configurations were tested. The color scheme represents the value of γ of the corresponding turbine. The horizontal line indicates the C_P value in the greedy configuration, while the pentagram denotes the column-optimal. (d) Magnified view of $C_{P,\mathrm{C3}}$ in the two last subgroups of configurations, in which $\gamma_1 = 18^\circ$ and $\gamma_1 = 21.6^\circ$.

best cases (relative to the farm power), the two downwind turbines account for $52.9\ \%$ of the total production in the left column and $53.6\ \%$ in the right one. In the central column, the share drops to $48.7\ \%$. As a reference, the six downwind turbines contribute to $42.7\ \%$ of the farm power in greedy operation. These findings suggest that the additional kinetic energy available to the downstream turbines, following yaw actuation, is more significant in the lateral columns, possibly because the energy entrainment can also occur from the undisturbed flow on the sides of the array. Conversely, in the central column, entrainment is largely confined to the region above the rotors and is less responsive to yaw control Therefore, the same conditions that affect the greedy efficiency of a column also influence the extent to which its performance may be improved by active-control strategies.

3.1.4 Yawing the third row

As discussed in Sect. 3.1, the farm power can be increased by yawing the trailing-row turbines. To illustrate this effect, Fig. 13 presents the variation in C_P of the turbines in the central column, as measured in EXP2. The turbine performance displays the same characteristics outlined in Sect. 3.1.1, namely the cosinusoidal decay of $C_{P,\mathrm{C1}}$ and the dual dependence of $C_{P,\mathrm{C2}}$ on γ_1 and γ_2. In addition, Fig. 13(c) shows that $C_{P,\mathrm{C3}}$ is only marginally affected by γ_3 at small values of γ_1. However, a distinct trend emerges on the right-hand side of the figure, where γ_1 is large: with constant γ_1 and γ_2, turbine C3 is less productive at $\gamma_3 = +5.4^\circ$ than at $\gamma_3 = 0^\circ$ and it is often more efficient at $\gamma_3 = -5.4^\circ$, i.e. when it is yawed in the opposite direction of the turbines upstream. This trend is further highlighted in Fig. 13(d) and mirrors the behaviour observed (in both experiments) for the second-row turbines, albeit with a reduced impact on the power coefficient. The same pattern is observed in the lateral columns.

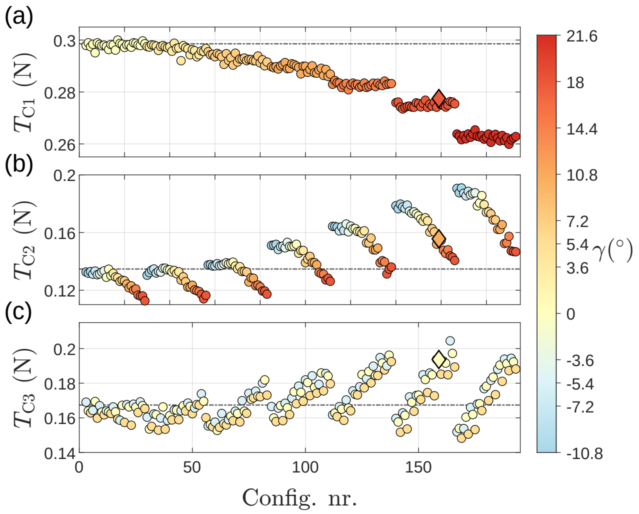

Figure 14. Thrust force measured on the turbines C1 (a), C2 (b) and C3 (c), measured in EXP2. The horizontal axis identifies the configuration number, following the chronological order in which the configurations were tested. The color scheme represents the value of γ of the corresponding turbine. The horizontal line indicates the thrust in the greedy configuration, while the diamond symbol denotes the farm-optimal configuration.

3.2 Thrust force

The turbine towers in the central columns were also equipped with strain gauges, serving as load cells. Figure 14 shows the axial component of the thrust force, T, measured in EXP2. Notably, the behaviour of T displays the same features as the C_P: T_{C1} is independent of the downstream conditions and decays as a cosine function of γ_1, while T_{C2} is largest, for a given γ_1, when C2 is yawed in the opposite direction. This further corroborates the hypothesis that, in Type 2 configurations, the wake deficit downstream of the the second turbine is large, leading to a reduced production in the third row. This is consistent with the findings of Bartl et al. (2018), who further reported a reduction of the yaw moments on the second turbine in this Type of configurations.

Furthermore, Figs. 15 and 16 display the impact of wake-steering control on the mean thrust force and its fluctuations, respectively, highlighting how these quantities change with increasing farm power. In most of the best-performing configurations, T_{C1} decreases while $\sigma_{T_{\mathrm{C1}}}$ increases compared to the greedy case. There are however several instances in which both quantities are lower while the farm power is higher than the baseline, indicating the possibility of a multi-objective optimization aimed at maximizing the power while minimizing the fatigue loads. In the case of turbine C2, the mean thrust and its fluctuations exhibit significant variations, but remain only moderately higher than the greedy value in the optimal cases. In contrast, both T_{C3} and $\sigma_{T_{\mathrm{C3}}}$ increase steadily with improving farm performance. Turbine C3 is also the one with the largest baseline fluctuation magnitude, which is expected as the turbulence intensity is known to increase further into the array. Relative to the mean thrust, the fluctuations grow progressively from one row to the next.

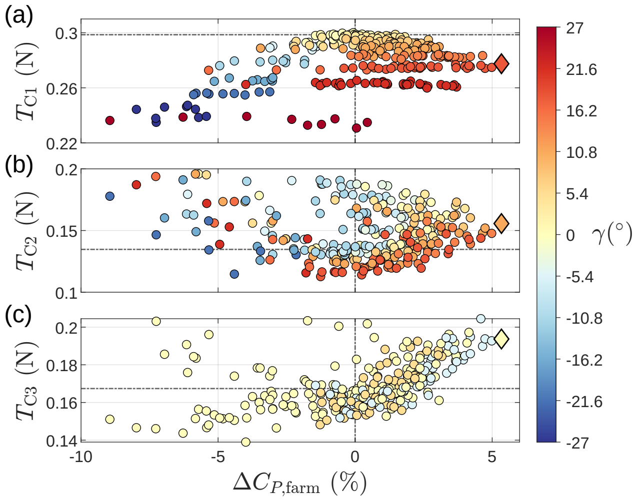

Figure 15. Scatter plot of the mean thrust force of turbines C1 (a), C2 (b) and C3 (c) versus the change in farm power coefficient. The data from both EXP1 and EXP2 are included. The color scheme represents the value of γ of the corresponding turbine. The horizontal solid lines indicate the T value in the greedy configuration, while the diamonds denote the farm-optimal case.

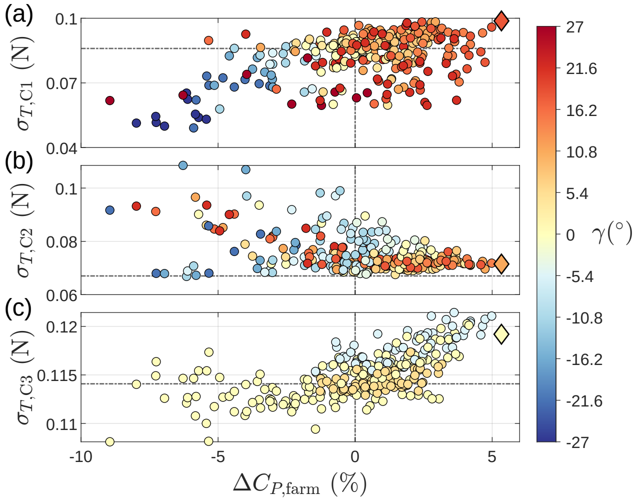

Figure 16. Scatter plot of the standard deviation of the thrust force time signals versus the change in farm power coefficient. The data correspond to turbine C1 (a), C2 (b) and C3 (c). Both EXP1 and EXP2 are included. The color scheme represents the value of γ of the corresponding turbine. The horizontal solid lines indicate the σ_T value in the greedy configuration, while the diamonds denote the farm-optimal case.

https://doi.org/10.5194/wes-2025-135
Preprint. Discussion started: 20 August 2025

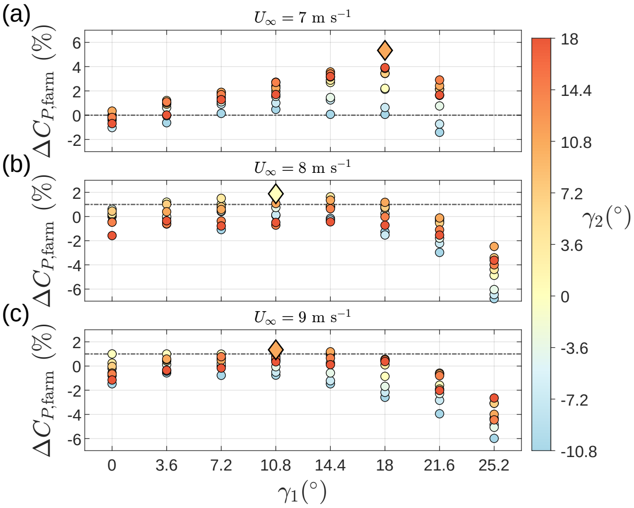

Figure 17. Farm power coefficient, normalized with its value in the greedy configuration, in three experiments with different free-stream velocities: (a) $U_\infty = 7\ \mathrm{m\,s^{-1}}$, (b) $U_\infty = 8\ \mathrm{m\,s^{-1}}$ and (c) $U_\infty = 9\ \mathrm{m\,s^{-1}}$. The abscissa and the color scheme denote the misalignment angles of the first and second rows, respectively. The diamonds indicates the respective farm-optimal configurations.

3.3 Effect of free-stream velocity

In order to investigate the influence of the free-stream velocity on the efficacy of wake-steering control, two additional experiments were performed with $U_\infty = 8$ and $9\ \mathrm{m\,s^{-1}}$. The corresponding U_hub are $6.88\ \mathrm{m\,s^{-1}}$ and $7.74\ \mathrm{m\,s^{-1}}$, respectively. The configurations evaluated here are the subset of those from EXP2 where $\gamma_3 = 0^\circ$, with the inclusion of one more possible value for γ_1, namely 25.2°. The values of $\Delta C_{P,\text{farm}}$ measured with the three velocities are compared in Fig. 17. The results indicate that the maximum power gain decreases with increasing U_∞. In fact, $\Delta C_{P,\text{farm}}$ falls from 5.3 % at $7\ \mathrm{m\,s^{-1}}$ to 1.9 % and 1.3 % at $8\ \mathrm{m\,s^{-1}}$ and $9\ \mathrm{m\,s^{-1}}$, respectively. A similar trend can be observed considering the changes in $C_{P,\text{col}}$, shown if Fig. 18(a), with the exception of left column, which experiences a larger improvement at $9\ \mathrm{m\,s^{-1}}$ than at $8\ \mathrm{m\,s^{-1}}$. The reduction in power gains can be partly explained by the fact that the farm $C_{P,\text{gr}}$, used as a reference, increases from 0.178 at $7\ \mathrm{m\,s^{-1}}$ to 0.192 at $8\ \mathrm{m\,s^{-1}}$ and to 0.198 at $9\ \mathrm{m\,s^{-1}}$. Thus the array in greedy conditions becomes more efficient with increasing free-stream velocity, which may limit the scope for improvement through control strategies. The additional power, however, is not uniformly distributed within the model farm. As seen in Figs. 18(b-d), the largest performance growth takes place in the first row of turbines, whose $C_{P,\text{gr}}$ increases on average by 14.5 % from $U_\infty = 7\ \mathrm{m\,s^{-1}}$ to $U_\infty = 9\ \mathrm{m\,s^{-1}}$. The baseline production of the second and third rows is only enhanced by 7.6 % (most of which is due to the power change of C2) and 6.1 %, respectively. This indicates that only a small amount of the additional kinetic energy available in the free stream is entrained deep into the array and can reach the downstream turbines. The change in C_P of the first row is likely caused by a Reynolds-number dependence of the turbines power characteristics. It is also possible that the ratio between U_∞ and U_hub may not be constant, as initially assumed, which would inflate (or deflate) the estimated undisturbed U_hub and thus the C_P. How-

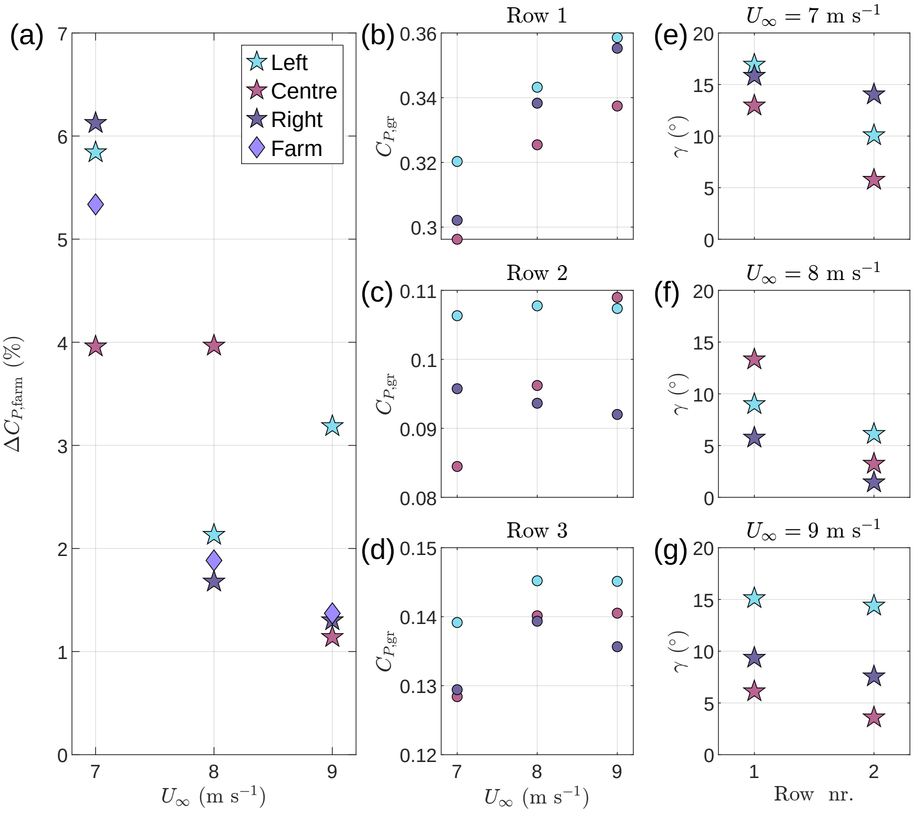

Figure 18. Maximum normalized change of power coefficient for the three columns and for the entire farm at the three free-stream velocities (a). Greedy power coefficients of the turbines in the first row (b), second row (c) and third row (d). Yaw angles of the turbines in the first two rows averaged among the 15 best cases relative to each column, with $U_\infty = 7\ \mathrm{m\,s^{-1}}$ (e), $U_\infty = 8\ \mathrm{m\,s^{-1}}$ (f) and $U_\infty = 9\ \mathrm{m\,s^{-1}}$ (g). The angle of the third row is not represented as $\gamma_3 = 0°$ in all cases.

ever, this would apply equally to the whole array and therefore does not explain the differences between rows. Even though the fraction of total power generated in the upstream row increases only modestly, from $57.3\ \%$ at $U_\infty = 7\ \mathrm{m\,s^{-1}}$ to $59\ \%$ at $U_\infty = 9\ \mathrm{m\,s^{-1}}$, it is sufficient to make it less advantageous to sacrifice performance of those turbines to benefit the ones downstream. The best-performing configurations at higher U_∞ are therefore characterized by smaller values of γ_1, as shown in Figs. 18(e-g), which makes them more similar to the greedy one. As a result, the maximum power increment among these cases is limited. This is analogous to what is observed, at $U_\infty = 7\ \mathrm{m\,s^{-1}}$, for the central column. As illustrated in Fig. 18(c), the C_P of turbine C2 is lower than that of L2 or R2. Consequently, it is less advantageous to forgo the production of turbine C1 to benefit C2, resulting in a smaller mean γ_1 in the best configurations for the central column compared to the others, as depicted in Fig. 18(e).

An additional remark can be made with regards to the optimal angles of the second row. As stated in Sect. 3.1, the optimal configurations are characterized by values of γ_2 that are smaller or, in some cases, equal to γ_1. Figures 18(e-g) reveal that the average γ_2 among the best cases decreases significantly from $U_\infty = 7\ \mathrm{m\,s^{-1}}$ to $8\ \mathrm{m\,s^{-1}}$, as expected. However, at $U_\infty = 9\ \mathrm{m\,s^{-1}}$, the optimal γ_2 of the lateral columns are once again large and comparable to the corresponding γ_1. This observation is consistent with the fact that the $C_{P,\mathrm{col}}$ of the left column improves more at $U_\infty = 9\ \mathrm{m\,s^{-1}}$ than at $8\ \mathrm{m\,s^{-1}}$ and it points to the nonlinear influence exerted by the free-stream velocity on the energy trade-offs taking place within the farm. Furthermore, the large values of γ_1 and γ_2 in the best configurations indicate that the lateral columns would probably experience an additional, non-negligible power gain from yawing the third row.

3.4 A note on the infinite-farm assumption

Since each column responds differently to a given yaw configuration, as discussed in Sect. 3.1.1, it is natural to wonder whether it is possible to achieve further power improvements by controlling each column independently. Thus, in the final experiment, the model farm was tested while yawing each column to one of the configurations that gave the best improvements of its respective $C_{P,\mathrm{col}}$. The 150 cases examined here come from all the possible combinations of the six best configurations for the left column and the five for the centre and right columns. These were chosen from EXP1 and EXP2, as we all some additional experiments that have not been presented in this work for the sake of brevity and because they do not provide further insights. The results indicate that the model farm does not experience further power gains compared to the configurations in which all the turbines in a row were yawed equally. The maximum improvement measured here was $\Delta C_{P,\mathrm{farm}} = 4.8\%$, which corresponds to the configuration with $\overline{\gamma_L} = (19.8°, 14.4°, -3.6°)$, $\overline{\gamma_C} = (18°, 3.6°, 0°)$ and $\overline{\gamma_R} = (18°, 16.2°, -7.2°)$. The range of yaw angles from the configurations tested in this experiment is too limited to draw comprehensive conclusions regarding the mutual influences that each column exerts on the others. Nonetheless, it was sufficient to observe that the right column tends to perform slightly better when the yaw angle of turbine L1 is large. This suggests that it may be worth conducting a parametric study on such influences, as they are likely to play a key role in wake-steering control of farms with close spanwise spacings between columns.

4 Comparison with results from the literature

The largest overall power gain reported in this work, $+5.3\%$, is considerably lower than some results found in the literature. Considering the differences between those experiments and ours may highlight some key aspects to consider when implementing wake-steering control.

The main difference between this work and that of Campagnolo et al. (2016) is that their three turbines were not positioned in an aligned column. Instead, each downstream rotor was offset by $0.5D$ in the spanwise direction relative to the one directly upstream. This meant that, for sufficiently large yaw angles of the first two turbines, the interaction of their wakes with the downstream turbines could almost entirely be removed, leading to larger power increments (up to 15%).

The comparison with the results of Bastankhah and Porté-Agel (2019) is of particular interest, given that the turbine geometries are very similar (see Sect. 2.2) while the turbine diameter and streamwise spacing are identical. Additionally, both experimental setups present an ABL inflow with comparable δ_{99}/D. The primary distinctions are that the hub velocity in their

https://doi.org/10.5194/wes-2025-135
Preprint. Discussion started: 20 August 2025

work is lower (4.8 vs $5.95\ \mathrm{m\,s^{-1}}$), as are their friction velocity u_τ and roughness length z_0, and that their array consists of a single column. When considering only the first three of their five turbines, Bastankhah and Porté-Agel (2019) achieved a power gain of 8%, with the first two turbines yawed by approximately $25°$ and $15°$, respectively. In our experiments, only the lateral columns come close to such improvements, with the left column improving by up to 5.8% and the right one up to 6.9%, as reported in Sect. 3.1.3. These shortcomings may be explained by the higher U_{hub} used here, in accordance with the discussion in Sect. 3.3. On the other hand, the stark discrepancy between our central column, which improves by only 4%, and the results of Bastankhah and Porté-Agel (2019) further emphasizes the impact the close spacing between columns on the efficacy of wake-steering control.

The study conducted by Rotea et al. (2024) offers a valuable comparison of the usefulness of yaw-control strategies applied to different multi-column wind-farm model. The power gain that they reported is about 9% and there are several differences between their experiment and ours that are worth examining. While both turbine geometries are based on the model proposed by Bastankhah and Porté-Agel (2017), their rotor has a larger diameter (0.2 vs $0.15\ \mathrm{m}$). Both the mean velocity and the turbulence intensity at hub height are higher in the setup of Rotea et al. (2024), which, according to our discussion in Sect. 3.3 and the findings of Bartl et al. (2018), should reduce the control efficacy. On the other hand, the spanwise distance between columns is larger in their case ($4D$ vs $2.67D$), and the additional turbine row is expected, based on the results of Bastankhah and Porté-Agel (2019), to enable additional performance improvements. An additional point of divergence, whose impact on wake steering is unknown, is the shear exponent of the ABL inflow, α, which is higher in their case, 0.2 vs 0.14. Their exponent is typically associated with rougher terrains and woodland areas Counihan (1975). It is important to note that Rotea et al. (2024) restricted their control actuation to two of the four rows, either the first and second or the first and third. Without this constraint, they might have measured even higher gains. Finally, another reason behind their greater improvements is that the power losses of their turbines in the first row, which are yawed by nearly $30°$, are only about 20%. In comparison, Fig. 11(a) illustrates that our first-row turbines, when yawed by similar angles, lose up to 30% of their power. Clearly, the increased sensitivity to yaw exhibited by our rotors affects the energy trade-offs between the turbine rows, limiting the potential power gains.

5 Conclusions

In this work, the impact of wake-steering control has been systematically tested by monitoring the performance of a model wind farm operating in a large number of yaw configurations. The largest measured power improvement was about $+5.3\%$, achieved with the angles $\overline{\gamma} = (18°, 10.8°, 0°)$. The response of the farm is asymmetric with respect to the direction of the yaw angle of the turbines in the first row, with only positive angles (counterclockwise when seen from an upstream perspective) leading to power gains. It is speculated that this is caused by the interaction of the wake rotation with the counter-rotating vortex pair that forms in yawed wakes. This interaction influences the magnitude of the lateral deflection and determines the direction of the vertical wake displacement, which may play a role in the energy tradeoffs that make wake-steering control strategies beneficial.

Considering the C_P of the individual turbines within one column, it is found that the power produced by the turbines in the second row is maximized when they are yawed in the opposite direction of the upstream rotors, i.e. a negative yaw. This leads to the identification of two Types of configurations: Type 1, where the first two rows are both yawed by positive angles and the power production is distributed more evenly throughout the farm; Type 2, in which the power is concentrated in the first two rows, maximizing the production of the turbines in the second row at the expense of the ones in the last row. It is found that, in general, Type 1 configurations lead to better results, with the maximum power increment recorded in a Type 2 configuration being $+3.3\%$ compared to the $+5.3\%$ in Type 1.

It is observed that the three columns of turbines respond differently to the same configuration and in particular that the lateral columns experience the largest improvements from wake steering. A possible explanation is that, for the lateral column, kinetic energy may be entrained both from above and from the edges of the array, whereas in the case of the central column this may be limited to the upper part of the wakes. Additionally, it is found that finely-tuned configurations, in which each row is yawed independently from the others according to the configurations that lead to the respective best results, do not yield additional power extraction. This is likely due to the nonlinear interaction between the columns and the incoming boundary-layer flow.

In addition, it is reported that the benefits of wake-steering tend to diminish with increasing free-stream velocity. This is partly caused by the increased efficiency measured at higher speeds in the baseline, greedy configuration and partly the fact that this improved performance is not uniformly distributed within the farm but it is concentrated in the turbines in the first row. The resulting change in the energy tradeoffs makes it less advantageous to yaw the first-row turbines by large angles and therefore limits the possible improvements to the farm power.

Finally, it is worth noting that the power improvements recorded in this work are lower than other examples found in the literature. This may be caused by a multitude of parameters concerning the experimental setups. One such parameter is the hub velocity, as demonstrated in this article. Other examples may include the turbines size, $C_{P,\max}$ and operating tip-speed ratio, the farm geometry and the properties of the ABL in the rotor-swept area, to name a few. Further investigations are therefore needed in order to determine which of these factors are more important in determining the maximum possible power improvements.

Data availability. The experimental data can be obtained by contacting the authors.

Author contributions. The project was conceptualized by AS. The wind-turbine models were designed by DM and AS. The hardware and software used to control and monitor the turbines was designed and built by DM. The devices used to replicate the atmospheric boundary layer were designed by DM and tested by DM, AS and JHMF. The wind-tunnel experiments were planned by DM, AS and JHMF and conducted by DM. The data analysis and interpretation was performed by DM and AS. The article was written by DM, AS and JHMF.

Competing interests. The authors declare no competing interests.

Acknowledgements. The project has been financed by the Swedish Energy Agency (grant nr. 48649-1).

References

Adaramola, M. and Krogstad, P.-Å.: Experimental investigation of wake effects on wind turbine performance, Renewable energy, 36, 2078–2086, 2011.

Bartl, J. and Sætran, L.: Experimental testing of axial induction based control strategies for wake control and wind farm optimization, in: J. Phys.: Conf. Ser., vol. 753, p. 032035, IOP Publishing, 2016.

Bartl, J., Mühle, F., and Sætran, L.: Wind tunnel study on power output and yaw moments for two yaw-controlled model wind turbines, Wind Energy Sci., 3, 489–502, https://doi.org/10.5194/wes-3-489-2018, 2018.

Bastankhah, M. and Porté-Agel, F.: Experimental and theoretical study of wind turbine wakes in yawed conditions, J. Fluid Mech., 806, 506–541, 2016.

Bastankhah, M. and Porté-Agel, F.: A new miniature wind turbine for wind tunnel experiments. Part I: Design and performance, Energies, 10, 908, 2017.

Bastankhah, M. and Porté-Agel, F.: Wind farm power optimization via yaw angle control: A wind tunnel study, J. Ren. Sust. Energy, 11, 023 301, https://doi.org/10.1063/1.5077038, 2019.

Bossanyi, E. and Ruisi, R.: Axial induction controller field test at Sedini wind farm, Wind Energy Science, 6, 389–408, 2021.

Bossuyt, J., Scott, R., Ali, N., and Cal, R. B.: Quantification of wake shape modulation and deflection for tilt and yaw misaligned wind turbines, J. Fluid Mech., 917, https://doi.org/doi:10.1017/jfm.2021.237, 2021.

Bottema, M.: Urban roughness modelling in relation to pollutant dispersion, Atmos. Env., 31, 3059–3075, 1997.

Bourhis, M., Pereira, M., Ravelet, F., and Dobrev, I.: Innovative design method and experimental investigation of a small-scale and very low tip-speed ratio wind turbine, Exp. Therm. Fluid Sci., 130, 110 504, https://doi.org/https://doi.org/10.1016/j.expthermflusci.2021.110504, 2022.

Burton, T., Jenkins, N., Sharpe, D., and Bossanyi, E.: Wind energy handbook, John Wiley & Sons, 2011.

Campagnolo, F., Petrović, V., Schreiber, J., Nanos, E. M., Croce, A., and Bottasso, C. L.: Wind tunnel testing of a closed-loop wake deflection controller for wind farm power maximization, J. Phys. Conf. Ser., 753, 032 006, 2016.

Clayton, B. R. and Filby, P.: Measured effects of oblique flows and change in blade pitch angle on performance and wake development of model wind turbines, in: Proc. 4th BWEA Wind Energy Conf., BHRA Fluid Eng., Cranfield, Bedford, UK, pp. 214–224, 1982.

Counihan, J.: An improved method of simulating an atmospheric boundary layer in a wind tunnel, Atmos. Environ., 3, 197–214, 1969.

Counihan, J.: Adiabatic atmospheric boundary layers: A review and analysis of data from the period 1880–1972, J. Atmos. Env., 9, 871–905, https://doi.org/10.1016/0004-6981(75)90088-8, 1975.

Dahlberg, J. and Medici, D.: Potential improvement of wind turbine array efficiency by active wake control (AWC), in: Proc. European Wind En. Conf. and Exhib., Madrid, Spain, 2003.

Fleming, P., Annoni, J., Churchfield, M., Martinez-Tossas, L. A., Gruchalla, K., Lawson, M., and Moriarty, P.: A simulation study demonstrating the importance of large-scale trailing vortices in wake steering, Wind Energy Sci., 3, https://doi.org/10.5194/wes-3-243-2018, 2018.

Hohman, T. C., Van Buren, T., Martinelli, L., and Smits, A.: Generating an artificially thickened boundary layer to simulate the neutral atmospheric boundary layer, J. Wind Eng. Ind. Aerodyn., 145, 1–16, 2015.

Howland, M. F., Bossuyt, J., Martínez-Tossas, L. A., Meyers, J., and Meneveau, C.: Wake structure in actuator disk models of wind turbines in yaw under uniform inflow conditions, J. Ren. Sust. Energy, 8, 2016.

Howland, M. F., Lele, S. K., and Dabiri, J. O.: Wind farm power optimization through wake steering, Proc. Nat. Acad. Sci., 116, 14 495–14 500, 2019.

Howland, M. F., Quesada, J. B., Martínez, J. J. P., Larrañaga, F. P., Yadav, N., Chawla, J. S., Sivaram, V., and Dabiri, J. O.: Collective wind farm operation based on a predictive model increases utility-scale energy production, Nature Energy, 7, 818–827, 2022.

International Energy Agency: World Energy Outlook 2024, https://www.iea.org/reports/world-energy-outlook-2024, licence: CC BY 4.0 (report); CC BY NC SA 4.0 (Annex A), 2024.

Jiménez, Á., Crespo, A., and Migoya, E.: Application of a LES technique to characterize the wake deflection of a wind turbine in yaw, Wind energy, 13, 559–572, 2010.

Lindgren, B. and Johansson, A. V.: Evaluation of the flow quality in the MTL wind-tunnel.Report TRITA-MEK, Dept. of Mechanics, KTH, 2002.

Mazzeo, F., Micheletto, D., Talamelli, A., and Segalini, A.: An Experimental Study on a Wind Turbine Rotor Affected by Pitch Imbalance, Energies, 2022.

McKay, P., Carriveau, R., and Ting, D. S.-K.: Wake impacts on downstream wind turbine performance and yaw alignment, Wind Energy, 16, 221–234, https://doi.org/https://doi.org/10.1002/we.544, 2013.

Medici, D. and Alfredsson, P. H.: Measurements on a wind turbine wake: 3D effects and bluff body vortex shedding, Wind Energy, 9, 219–236, 2006.

Meyers, J., Bottasso, C., Dykes, K., Fleming, P., Gebraad, P., Giebel, G., Göçmen, T., and Wingerden, J. W.: Wind farm flow control: prospects and challenges, Wind Energy Sci., https://doi.org/10.5194/wes-2022-24, 2022.

Micheletto, D., Fransson, J. H. M., and Segalini, A.: Experimental Study of the Transient Behavior of a Wind Turbine Wake Following Yaw Actuation, Energies, 16, https://doi.org/10.3390/en16135147, 2023a.

Micheletto, D., Segalini, A., and Fransson, J. H. M.: Experimental analysis of the wake behind a small wind-turbine model in yaw, J. Phys.: Conf. Ser., 2505, 012 030, https://doi.org/10.1088/1742-6596/2505/1/012030, 2023b.

Rotea, M. A., Kumar, D., Aju, E. J., and Jin, Y.: Multi-row extremum seeking for wind farm power maximization, J. Phys. Conf. Ser., 2767, 032 043, https://doi.org/10.1088/1742-6596/2767/3/032043, 2024.

van der Hoek, D., Kanev, S., Allin, J., Bieniek, D., and Mittelmeier, N.: Effects of axial induction control on wind farm energy production-a field test, Renewable energy, 140, 994–1003, 2019.

Veers, P., Dykes, K., Lantz, E., Barth, S., Bottasso, C. L., Carlson, O., Clifton, A., Green, J., Green, P., Holttinen, H., Laird, D., Lehtomäki, V., Lundquist, J. K., Manwell, J., Marquis, M., Meneveau, C., Moriarty, P., Munduate, X., Muskulus, M., Naughton, J., Pao, L., Paquette, J., Peinke, J., Robertson, A., Rodrigo, J. S., Sempreviva, A. M., Smith, J. C., Tuohy, A., and Wiser, R.: Grand challenges in the science of wind energy, Science, 366, eaau2027, https://doi.org/10.1126/science.aau2027, 2019.

Wang, C., Wang, J., Campagnolo, F., Carraón, D. B., and Bottasso, C. L.: Validation of large-eddy simulation of scaled waked wind turbines in different yaw misalignment conditions, J. Phys.: Conf. Ser., 2018.

Zong, H. and Porté-Agel, F.: Apoint vortex transportation model for yawed wind turbine wakes, J. Fluid Mech., 890, https://doi.org/doi:10.1017/jfm.2020.123, 2020.

Österlund, J., Johansson, A., Nagib, H., and Hites, M.: A note on the overlap region in turbulent boundary layers, Phys. Fluids, 12, https://doi.org/10.1063/1.870250, 2000.